

Reduced basis methods for numerical room acoustic simulations with parametrized boundaries

Hermes Sampetro Llopis^{a,b}, Allan P. Engsig-Karup^c, Cheol-Ho Jeong^b, Finnur Pind^d, Jan S. Hesthaven^e

^a*Rambøll Denmark, Copenhagen, Denmark*

^b*Acoustic Technology Group, Department of Electrical Engineering, Technical University of Denmark, Kongens Lyngby, Denmark*

^c*Scientific Computing Section, Department of Applied Mathematics and Computer Science, Technical University of Denmark, Kongens Lyngby, Denmark*

^d*Treble Technologies, Reykjavík, Iceland*

^e*Chair of Computational Mathematics and Simulation Science, Ecole Polytechnique Federale de Lausanne, Lausanne, Switzerland*

Abstract

The use of model-based numerical simulation of wave propagation in rooms for engineering applications requires that acoustic conditions for multiple parameters are evaluated iteratively and this is computationally expensive. We present a reduced basis methods (RBM) to achieve a computational cost reduction relative to a traditional full order model (FOM), for wave-based room acoustic simulations with parametrized boundary conditions. In this study, the FOM solver is based on the spectral element method, however other numerical methods could be applied. The RBM reduces the computational burden by solving the problem in a low-dimensional subspace for parametrized frequency-independent and frequency-dependent boundary conditions. The problem is formulated and solved in the Laplace domain, which ensures the stability of the reduced order model based on the RBM approach. We study the potential of the proposed RBM framework in terms of computational efficiency, accuracy and storage requirements and we show that the RBM leads to 100-fold speed-ups for a 2D case with an upper frequency of 2kHz and around 1000-fold speed-ups for an analogous 3D case with an upper frequency of 1kHz. While the FOM

Email address: hs11o@elektro.dtu.dk (Hermes Sampetro Llopis)

simulations needed to construct the ROM are expensive, we demonstrate that despite this cost, the ROM has a potential of three orders of magnitude faster than the FOM when four different boundary conditions are simulated per room surface. Moreover, results show that the storage model for the ROM is relatively high but affordable for the presented 2D and 3D cases.

Keywords: Room acoustic simulations; model order reduction; reduced basis methods; Laplace domain; complex boundaries.

1. Introduction

Room acoustic simulations are used for various purposes, e.g., building design, music, hearing research, entertainment, and virtual reality (VR). Historically, these simulations have mostly been carried out by means of geometrical acoustics (GA) methods [1, 2], such as ray tracing, which approximate the sound propagation to ensure a manageable computational cost, but fails to simulate the correct wave nature of sound, resulting in diffraction and interference at low frequencies. The geometric approximation is known to cause a considerable degradation of the simulation accuracy in many cases [3]. Another approach is to numerically solve the governing equations, i.e., the wave equation in the time-domain or the Helmholtz equation in the frequency domain, using numerical discretization methods. Different numerical methods have been applied to the room acoustics problem in the past, e.g., the finite element method (FEM) [4, 5], the spectral element method (SEM) [6], the finite difference method (FDTD) [7], the boundary element method (BEM) [8] and the discontinuous Galerkin finite element method (DG-FEM) [9]. These numerical methods are, in principle, more accurate than GA, as no approximation on the wave propagation is introduced except for numerical errors by the discretization.

The main drawback of a wave-based modelling approach is the high computational cost, especially when modeling large spaces at higher frequencies. This makes it difficult to apply them to scenarios where the full audible spectrum and large room dimensions must be considered, e.g., simulating a large hall from

20 Hz to 20 kHz. A wave-based simulation of a large hall up to 20 kHz remains very challenging, and the goal of this study is not to propose a methodology that
25 enables this. Instead, we consider the case where the same room is simulated multiple times under varying boundary conditions. This type of use case is very common in e.g. building design, where different surface materials are tested to identify desired acoustic conditions. Thus, reducing the computation time for the parameterized boundary condition case is of utmost importance for many
30 applications.

We propose a computational framework to reduce the computational cost compared to traditional *full-order* numerical solutions. The framework is based on a reduced basis method (RBM) for the acoustics problem that includes parametrization of key design parameters at the boundary of the domain. It
35 can be applied e.g. to surface absorption and scattering, and enables a substantial cost reduction when simulating a room multiple times under parameter variation at the boundaries.

Any full-order numerical solver can be used in the RBM framework to capture the underlying physics needed to build the reduced basis. It is relevant to
40 impose the following requirements; 1) geometric flexibility, which allows simulation of curved and complex geometries, 2) high-order accuracy to minimize wave dispersion over long distances, 3) transient response reconstruction, i.e., impulse response, 4) a stable reduced order model (ROM) and 5) the possibility to extend the applicability to large spaces and high frequencies. To fulfill 1)
45 methods such as FDTD with structured grids are not well suited. Instead, FEM, BEM, SEM or DG-FEM provide geometric flexibility, which is needed in room acoustics to accurately model complex shaped rooms, i.e. curved geometries [6]. Requirement 2) can be fulfilled by any high-order scheme. SEM and DG-FEM are examples of numerical methods that lend themselves naturally to high-order
50 discretizations [10] with low dispersion and dissipation properties [11–13]. To fulfill 3) time-domain (TD) and Laplace domain (LD) are more suitable than Fourier-domain (FD). In particular, when solving the problem in the frequency domain, LD is more appropriate for non-periodic problems with a transient re-

sponse. In terms of requirement 4) TD approaches are known to be challenging
55 when it comes to stability robustness of reduced order modeling frameworks
[14–17]. Finally, 5) requires scalable methods, ideally of $\mathcal{O}(N)$, where N is the
total degrees of freedom in the scheme. Considering these desired features, we
have chosen to work with the spectral element method for the full-order model
solver in the Laplace domain. When compared against DG-FEM, the SEM is
60 simpler when solving in the Laplace domain, while DG-FEM requires definition
of the fluxes [18, 19] and results in larger discrete problems. But we highlight
again that any numerical framework could be used for the full order model.

RBM represents an emerging field of numerical techniques for efficiently
solving parametrized problems when a large number of model-based simulations
65 with different parameter values are needed [20–28]. RBM have been successfully
applied in many different fields, e.g., computational fluid dynamics [29, 30],
electromagnetics [31, 32], heat transfer [33] and vibroacoustics [34–36]. However,
the method has been applied to the wave equation only in a few studies [37–42].
The RBM consists of two stages; An offline stage where the parameter space
70 is explored to generate a problem-dependent basis using the full order model
solver, and a Galerkin projection to reduce the dimensionality of the problem
by utilizing the generated basis. The Galerkin projection requires access to
the code, hence, it is referred to as an intrusive technique. An online stage,
enables the problem to be solved for the new parameter value at a much lower
75 computational cost by evaluating the reduced problem. The generation of the
basis can be seen as a data-driven technique that relies on a proper orthogonal
decomposition (POD). This offline stage is typically computationally costly as
it requires multiple full order solutions, to produce so-called “snapshots” that
capture relevant states for different parameters. The reduction of the size of the
80 computational problem then comes with the truncation of the basis, which may
be a source of numerical instability in the reduced model even when the full
order model (FOM) is stable [14]. A critical challenge in RBM techniques is the
instability issue that may appear in long time numerical simulations if not taken
care of in the formulation of the method. Some remedies have been proposed

85 to address the instability in the time-domain [39, 43–45]. A previous study solves and reduces the acoustic-elastic wave equation in the Laplace domain to ensure stability [38]. One challenge for the Laplace domain method is the time signal reconstruction, which is important in acoustics for computing the different acoustic parameters [46], playback and auralization purposes [2]. In 90 Addition, the combination of RBM and SEM, has been investigated in other areas, e.g., for the Navier-Stokes equations [47, 48], where a potential synergy between high-order discretization and reduced basis methods is demonstrated.

The main novelty and contribution of this study is twofold: 1) it derives a 2D and 3D RBM framework formulated in the Laplace domain for the room acoustic 95 problem with parameterized frequency-independent and frequency-dependent boundary conditions and 2) it provides a detailed analysis of the potential and drawbacks of the framework for room acoustic simulations.

2. Method description

2.1. Full Order Model in Laplace domain

The acoustic wave propagation in a lossless and steady medium is described by the second-order wave equation,

$$\frac{\partial^2 \hat{p}}{\partial t^2} - c^2 \Delta \hat{p} = 0, \quad \text{in } \Omega \times (0, T], \quad (1)$$

where $\hat{p}(\mathbf{x}, t)$ is the sound pressure, $\mathbf{x} \in \Omega$ the position in the domain $\Omega \subset \mathbb{R}^d$ with $d = 2, 3$, t is the time in the interval $(0, T]$ s and c is the speed of sound ($c = 343$ m/s). The second-order equation can also be written as a system of two coupled linear first-order partial differential equations

$$\frac{\partial \hat{\mathbf{v}}}{\partial t} = -\frac{1}{\rho} \nabla \hat{p}, \quad \text{in } \Omega \times (0, T], \quad (2a)$$

$$\frac{\partial \hat{p}}{\partial t} = -\rho c^2 \nabla \cdot \hat{\mathbf{v}}, \quad (2b)$$

100 where $\hat{\mathbf{v}}(\mathbf{x}, t)$ is the particle velocity and ρ is the density of the medium ($\rho = 1.2$ kg/m³). The system can be excited with an initial condition, e.g., a Gaussian

pulse with a spatial variance σ_g for the sound pressure, and zero for the particle velocity.

In this study, a Laplace domain approach is considered. The time-dependent problem can be reduced to the computation of the Laplace transform of the sound pressure evaluated at a fixed complex frequency $s = \sigma + i\gamma$, by multiplying (1) by e^{-st} and integrating in time over the interval $[0, \infty)$ to obtain

$$s^2 p - c^2 \Delta p = s \hat{p}_0 + \hat{p}_{t,0}, \quad (3)$$

where $p(\mathbf{x}, s)$ is the Laplace transform of $\hat{p}(\mathbf{x}, t)$, $\hat{p}_0(\mathbf{x}) = \hat{p}(\mathbf{x}, t = 0)$ is the initial condition in the time-domain and $\hat{p}_{t,0}(\mathbf{x}) = \left. \frac{\partial \hat{p}(\mathbf{x}, t)}{\partial t} \right|_{t=0}$. A Gaussian pulse is considered,

$$\hat{p}_0(\mathbf{x}) = e^{-\left(\frac{\mathbf{x}-\mathbf{x}_0}{\sigma_g}\right)^2}, \quad \hat{p}_{t,0}(\mathbf{x}) = 0, \quad (4)$$

where \mathbf{x}_0 is the position of the source and σ_g is the spatial variance. Note that
105 the Laplace transform of $\hat{\mathbf{v}}(\mathbf{x}, t)$ will be denoted by $\mathbf{v}(\mathbf{x}, s)$.

To solve (3) numerically, the spatial derivatives are discretized and each complex frequency is evaluated separately. By multiplying (3) with a test function w , integrating over the domain and making use of Green's first identity, we obtain the weak formulation

$$\int_{\Omega} s^2 p w d\Omega + \int_{\Omega} c^2 \nabla p \cdot \nabla w d\Omega - \oint_{\Gamma} c^2 \frac{\partial p}{\partial \mathbf{n}} w d\Gamma = \int_{\Omega} s \hat{p}_0 w d\Omega, \quad (5)$$

where \mathbf{n} is the outward pointing normal vector of the boundary Γ of Ω . For harmonic signals, the conservation of momentum yields a proportional relation between the surface normal pressure derivative ($\frac{\partial p}{\partial \mathbf{n}}$) and the surface normal velocity at the boundary ($v_n = \mathbf{v} \cdot \mathbf{n}$) given by $\frac{\partial p}{\partial \mathbf{n}} = -\rho p v_n$. In room acoustics it is common to define the boundary conditions in terms of the surface impedance Z_s [49]. The normal incidence absorption coefficient α_{norm} can be obtained

from the surface impedance as follows

$$\alpha_{norm} = 1 - \left| \frac{Z_s - \rho c}{Z_s + \rho c} \right|^2. \quad (6)$$

Given the relation $Z_s = p_\Gamma/v_n$, the impedance boundary condition can be written

$$\frac{\partial p}{\partial \mathbf{n}} = -s\rho \frac{p_\Gamma}{Z_s}, \quad (7)$$

where p_Γ denotes the sound pressure at the boundary. Substituting (7) into (5) allows elimination of the normal pressure in the boundary integrals

$$\begin{aligned} \int_{\Omega} s^2 p w d\Omega + \int_{\Omega} c^2 \nabla p \cdot \nabla w d\Omega \\ + \oint_{\Gamma} s c^2 \frac{\rho}{Z_s} p_\Gamma w d\Gamma = \int_{\Omega} s \hat{p}_0 w d\Omega. \end{aligned} \quad (8)$$

The SEM formulation is well known, an overview and the definition of the operators can be found [6, 50, 51]. The formulation written in the Laplace domain is given by

$$(s^2 \mathcal{M} + c^2 \mathcal{S} + s c^2 \frac{\rho}{Z_s} \mathcal{M}_\Gamma) \mathbf{p} = s \hat{p}_0 \mathcal{M}, \quad (9)$$

where $\mathcal{M} \in \mathbb{R}^{N \times N}$ is the mass matrix, $\mathcal{S} \in \mathbb{R}^{N \times N}$ is the stiffness matrix and N denotes the degrees of freedom (DOF). The stiffness matrix for 2D is given by $\mathcal{S} = \mathcal{S}_x + \mathcal{S}_y$ and for 3D is $\mathcal{S} = \mathcal{S}_x + \mathcal{S}_y + \mathcal{S}_z$. Here the x, y, z subscripts denote differentiation in Cartesian directions, respectively. It is important for the implementation to split (9) into a set of $2N$ real equations for a given frequency $s = \sigma + i\gamma \in \mathbb{C}$, where the solution is written as $\mathbf{p} = \mathbf{p}^\sigma + i\mathbf{p}^\gamma$ [38]. After simple manipulations, the system can be written as

$$(\mathbf{K}^\sigma \mathbf{p}^\sigma - \mathbf{K}^\gamma \mathbf{p}^\gamma) + i(\mathbf{K}^\gamma \mathbf{p}^\sigma + \mathbf{K}^\sigma \mathbf{p}^\gamma) = \mathbf{Q}^\sigma + i\mathbf{Q}^\gamma, \quad (10)$$

where

$$\mathbf{K}^\sigma = (\sigma^2 - \gamma^2)\mathcal{M} + c^2\mathcal{S} + \sigma\mathcal{B}, \quad (11a)$$

$$\mathbf{K}^\gamma = 2\sigma\gamma\mathcal{M} + \gamma\mathcal{B}, \quad (11b)$$

$$\mathbf{Q}^\sigma = \sigma\hat{p}_0\mathcal{M}, \quad (11c)$$

$$\mathbf{Q}^\gamma = \gamma\hat{p}_0\mathcal{M} \quad (11d)$$

$$\mathcal{B} = c^2 \frac{\rho}{Z_s} \mathcal{M}_\Gamma. \quad (11e)$$

Finally, (10) can be written as

$$\begin{bmatrix} \mathbf{K}^\sigma & -\mathbf{K}^\gamma \\ \mathbf{K}^\gamma & \mathbf{K}^\sigma \end{bmatrix} \begin{bmatrix} \mathbf{p}^\sigma \\ \mathbf{p}^\gamma \end{bmatrix} = \begin{bmatrix} \mathbf{Q}^\sigma \\ \mathbf{Q}^\gamma \end{bmatrix}. \quad (12)$$

Note that for perfectly rigid boundaries, the particle velocity at the boundaries is $v_n = 0$, thus, $\mathcal{B} = 0$ and (9) reduces to

$$(s^2\mathcal{M} + c^2\mathcal{S})\mathbf{p} = s\hat{p}_0\mathcal{M}. \quad (13)$$

110 2.1.1. Frequency-dependent boundary condition

The frequency-dependent boundary conditions are implemented via the method of auxiliary differential equations (ADE) [6, 52, 53]. The sound pressure $p_\Gamma(\omega)$ and the normal velocity $v_n(\omega)$ at the boundaries are related through the relationship in the Fourier-domain

$$v_n(\omega) = \frac{p_\Gamma(\omega)}{Z_s(\omega)} = p_\Gamma(\omega)Y_s(\omega), \quad (14)$$

where ω is the angular frequency and $Z_s(\omega)$ is the surface impedance at the boundary. The admittance at the boundary $Y_s(\omega)$, is the inverse of $Z_s(\omega)$, which can be approximated as a rational function of order Q as

$$Y_s(\omega) = \frac{a_0 + \dots + a_Q(-i\omega)^Q}{1 + \dots + b_Q(-i\omega)^Q}, \quad (15)$$

and can be written as

$$\begin{aligned}
Y_s(\omega) &= Y_\infty + \sum_{k=1}^L \frac{A_k}{\hat{\lambda}_k - i\omega} \\
&+ \sum_{k=1}^S \left(\frac{B_k + iC_k}{\hat{\alpha}_k + i\hat{\beta}_k - i\omega} + \frac{B_k - iC_k}{\hat{\alpha}_k - i\hat{\beta}_k - i\omega} \right).
\end{aligned} \tag{16}$$

Hence L is the number of real poles $\hat{\lambda}_k$, S are the number of complex conjugate pole pairs $\hat{\alpha}_k \pm i\hat{\beta}_k$, used in the rational function approximation, and Y_∞ , A_k , B_k and C_k are coefficients. Applying the inverse Fourier transform and inserting the particle velocity definition, we recover the final expression

$$\begin{aligned}
\hat{v}_n(t) &= Y_\infty \hat{p}_\Gamma(t) + \sum_{k=1}^L A_k \hat{\phi}_k(t) \\
&+ \sum_{k=1}^S 2 \left[B_k \hat{\psi}_k^{(1)}(t) + C_k \hat{\psi}_k^{(2)}(t) \right],
\end{aligned} \tag{17}$$

where $\hat{\phi}_k$, $\hat{\psi}_k^{(1)}$ and $\hat{\psi}_k^{(2)}$ are the so called accumulators that can be determined by solving the corresponding differential equations [53]. Transforming the expressions to the Laplace domain yields

$$\hat{\phi}_k(s) = p_\Gamma(s)(s + \hat{\lambda}_k)^{-1}, \tag{18a}$$

$$\hat{\psi}_k^{(2)}(s) = \hat{\beta}_k p_\Gamma(s) [(s + \hat{\alpha}_k)^2 + \hat{\beta}_k^2]^{-1}, \tag{18b}$$

$$\hat{\psi}_k^{(1)}(s) = (s + \hat{\alpha}_k) \hat{\beta}_k^{-1} \hat{\psi}_k^{(2)}(s). \tag{18c}$$

115 The auxiliary differential equations to be solved can be written in matrix form for the real and imaginary parts by considering $s = \sigma + i\gamma$

$$\begin{bmatrix} \mathbf{G}^\sigma & -\mathbf{G}^\gamma \\ \mathbf{G}^\gamma & \mathbf{G}^\sigma \end{bmatrix} \begin{bmatrix} \hat{\phi}^\sigma \\ \hat{\phi}^\gamma \end{bmatrix} = \begin{bmatrix} p_\Gamma^\sigma \\ p_\Gamma^\gamma \end{bmatrix}, \tag{19}$$

where $\mathbf{G}^\sigma = \sigma + \hat{\lambda}_k$ and $\mathbf{G}^\gamma = \gamma$. Moreover,

$$\begin{bmatrix} \mathbf{G}^\sigma & -\mathbf{G}^\gamma \\ \mathbf{G}^\gamma & \mathbf{G}^\sigma \end{bmatrix} \begin{bmatrix} \hat{\psi}^{(2)\sigma} \\ \hat{\psi}^{(2)\gamma} \end{bmatrix} = \hat{\beta} \begin{bmatrix} p_\Gamma^\sigma \\ p_\Gamma^\gamma \end{bmatrix}, \tag{20}$$

where $\mathbf{G}^\sigma = \sigma^2 - \gamma^2 + 2\alpha\sigma + \hat{\alpha}^2 + \hat{\beta}^2$ and $\mathbf{G}^\gamma = 2\sigma\gamma + 2\hat{\alpha}\gamma$. Finally, $\hat{\psi}^{(1)}(s)$ can be obtained by substituting $\hat{\psi}^{(2)}(s)$ into (18c),

$$\hat{\psi}^{(1)\sigma} = \frac{1}{\hat{\beta}} \left[(\sigma + \hat{\alpha})\hat{\psi}^{(2)\sigma} - \gamma\hat{\psi}^{(2)\gamma} \right], \quad (21a)$$

$$\hat{\psi}^{(1)\gamma} = \frac{1}{\hat{\beta}} \left[\gamma\hat{\psi}^{(2)\sigma} + (\sigma + \hat{\alpha})\hat{\psi}^{(2)\gamma} \right]. \quad (21b)$$

Note that there is not a direct way to transform from the Fourier-domain to the Laplace domain. Thus, a procedure to solve the system, including the frequency-dependent boundaries, is described in Algorithm 1. First, the pressure is obtained from (13). Second, the real and imaginary part of the particle velocity at the boundaries is calculated by (17). Third, the admittance at the boundaries is calculated using the computed pressure and normal velocity at the boundary

$$\begin{aligned} Y_s &= Y_s^\sigma + iY_s^\gamma = \frac{v_n}{p_\Gamma} \\ &= \frac{v_n^\sigma p_\Gamma^\sigma + v_n^\gamma p_\Gamma^\gamma}{(p_\Gamma^\sigma)^2 + (p_\Gamma^\gamma)^2} + i \frac{v_n^\gamma p_\Gamma^\sigma - v_n^\sigma p_\Gamma^\gamma}{(p_\Gamma^\sigma)^2 + (p_\Gamma^\gamma)^2}. \end{aligned} \quad (22)$$

In this study we consider porous materials as frequency-dependent boundary conditions. The surface impedance can be estimated using Miki's model [54] in conjunction with a transfer matrix method [55], and mapped to a four pole rational function by using a vector fitting algorithm [56]. Finally, the sound pressure in the domain is solved with (12) where

$$\mathbf{K}^\sigma = (\sigma^2 - \gamma^2)\mathcal{M} + c^2\mathcal{S} + \sigma\mathcal{B}^\sigma, \quad (23a)$$

$$\mathbf{K}^\gamma = 2\sigma\gamma\mathcal{M} + \gamma\mathcal{B}^\gamma, \quad (23b)$$

$$\mathcal{B}^\sigma = c^2\rho(\sigma Y_s^\sigma - \gamma Y_s^\gamma)\mathcal{M}_\Gamma, \quad (23c)$$

$$\mathcal{B}^\gamma = c^2\rho(\gamma Y_s^\sigma + \sigma Y_s^\gamma)\mathcal{M}_\Gamma. \quad (23d)$$

Note that since Y_s has the same value in the whole boundary, it is sufficient to compute steps 1 to 7 for a single boundary node.

2.2. Time-domain signal reconstruction

In room acoustics the impulse responses are widely used to characterize a room for a given source and receiver pair. Temporal representations of audio

Algorithm 1 Frequency-dependent boundary conditions

```

1: procedure SOLVER
2:   Approximate  $Y_s$  (Miki's model) using the vectfit3 algorithm (16)
3:   for  $n = 1$  to  $N_s$  do
4:     Compute  $p_{\Gamma}^{\sigma}$  and  $p_{\Gamma}^{\gamma}$ , the pressure at the boundary defined in (13)
5:     Compute the accumulators by solving (19), (20) and (21)
6:     Compute  $v_n^{\sigma}$  and  $v_n^{\gamma}$  defined in (17)
7:     Compute the admittance at the boundary  $Y_s$  given in (22)
8:     Compute the pressure  $p$  by solving (12)
   return  $p^{\sigma}, p^{\gamma}$ 

```

signals are crucial in room acoustic simulations, particularly for playback and auralization purposes. Moreover, the impulse response is used to extract different room acoustic parameters [46]. The time reconstruction can be performed with the inverse Laplace transform. Since the analytical solution of the Laplace inverse transform is difficult to evaluate, the Weeks method is used to recover the time-dependent signal [57]. The temporal reconstruction by Weeks method depends on free parameters (σ, b) and number of complex evaluated frequencies N_s . The time signal can be expressed following the same approach as described in [38]

$$\hat{p}(t) = e^{(\sigma-b)t} \sum_{k=0}^{N_s-1} \hat{a}_k L_k(2bt), \quad (24)$$

where t denotes a time instant, $L_k(\cdot)$ is the Laguerre polynomial of degree $k = 0, \dots, N_s - 1$, which can be computed recursively using Clenshaw's algorithm [58]. The approximate expansion coefficients denoted by \hat{a}_k , depend on the Laplace solution and can be approximated as

$$\hat{a}_k = \frac{b}{N_z} \sum_{j=-N_s}^{N_s-1} \frac{e^{-ik\theta_{j+1/2}}}{1 - e^{i\theta_{j+1/2}}} p(s_j), \quad (25)$$

where $k = 0, \dots, N_s - 1$. The complex frequency is given by

$$s_j = \sigma + i\gamma = \sigma + ibg(\theta), \quad (26a)$$

$$g(\theta) = \frac{\cot(\theta_{j+1/2})}{2}, \quad \text{for } j = -N_s, \dots, N_s - 1, \quad (26b)$$

where $\theta_j = j\pi/N_s$, $\theta_{j+1/2} = (j + 1/2)\pi/N_s$. To improve the efficiency of the solver, two different polynomial orders can be chosen depending on the complex frequency

$$P_l \quad \text{for} \quad |g(\theta)| \simeq 0, \quad P_h \quad \text{for} \quad |g(\theta)| \gg 1. \quad (27)$$

By trigonometric identities it can be shown that by computing only the solution for $j = -N_s, \dots, -1$, a reduction in the number of required solutions is possible. Thus, the expression of $p(s_j)$ in (25) can be substituted by

$$p(s_j) = p_j^\sigma + ip_j^\gamma, \quad \text{for} \quad j = 0, \dots, N_s - 1, \quad (28a)$$

$$p(s_k) = p_k^\sigma - ip_k^\gamma, \quad \text{for} \quad k = 2N_s - j + 1, \quad (28b)$$

120 where $j = 0, \dots, N_s - 1$.

The choice of the free parameters (σ, b) can compromise the final results. A suboptimal choice may lead to large deviations from the actual solution. Moreover, choosing larger values of N_s than optimal, would avoid deviations but may lead to a longer computational time. There are different rules of thumb to find the optimum values for these parameters [59, 60], but as discussed in [38], none of them are convenient for this particular case. Following the approach presented in [38], the parameters are chosen by fixing a given resolution N_s , a number of time steps N_t and computing the solution for different parameter values that are compared with an analytical solution or a high fidelity time solver solution [6]. Hence

$$\sigma^{opt}, b^{opt} = \min_{\sigma, b} \left\| \sum_i (\hat{p}_i^*(\mathbf{x}, t) - p_i^*(\mathbf{x}, t)) \right\|_2^2, \quad (29)$$

where $\hat{p}_i^*(\mathbf{x}, t)$ is the solution obtained with a time solver and $p_i^*(\mathbf{x}, t)$ is the solution obtained by (24). A way to determine the number of complex frequencies N_s is to select the value that provides the same error as obtained with the time solver. Once the parameters are found for the FOM, they can be used also for

125 the RBM.

2.3. Reduced Order Model

The main motivation for reduced basis methods is to obtain a sufficiently accurate solution to a parametrized problem, for any value of the given parameter, at a reduced computational cost compared to the original high-fidelity solver. The method consists of two stages. First an offline stage a set of high-fidelity solutions, called snapshots, are computed for a selected set of parameter values to capture the relevant physics. The evaluation of the FOM for multiple parameter values results in a upfront computational cost and is used to generate N_{rb} basis functions by using, e.g., Proper Orthogonal Decomposition (POD). A Galerkin projection of the original problem results in a reduced problem with $N_{rb} \ll N$ degrees of freedom. During the online stage a system of dimension N_{rb} is solved for each new parameter value and the solution is recovered by a linear combination of the pre-generated basis functions. The key challenge of the method is to construct a reduced basis that preserves the physics dynamics for a required accuracy level. The high-fidelity solutions $p_{fb}(\mathbf{x}, s, \mu) = p^T$ of the parametrized problem under the variation of the parameter μ , belonging to the parameter space \mathbb{P} , approximates the solution manifold

$$M = \{p(\mu) | \mu \in \mathbb{P}\}, \quad (30)$$

The ultimate goal of the method is to approximate any part of the solution manifold with a small number of basis functions $\{\phi_i\}_{i=1}^{N_{rb}}$. Thus, the reduced space is a linear approximation of the solution manifold as $\mathbb{V}_{fb} = \text{span}\{\phi_1, \dots, \phi_{N_{rb}}\}$. The solution of the PDE is expressed as an expansion of the reduced basis functions $\phi_i(x)$ and the coefficients $a_i(s)$ in the Laplace domain,

$$p_{FOM}(x, s, \mu) \approx p_{ROM}(x, s, \mu) = \sum_{i=1}^{N_{rb}} \phi_i(x) a_i(s, \mu). \quad (31)$$

POD is a standard way to generate basis functions and it is used for data compression and low-dimensional approximations and provides an orthogonal basis. The reduced basis is obtained by truncating the basis while keeping the essential information that ensures the desired accuracy of the results. The

generation of the basis consists of performing a sampling of the parameter space $\mathbb{P}_h \subset \mathbb{P}$ for $[\mu_1, \dots, \mu_{N_\mu}]$. The snapshots are collected into a snapshot matrix

$$\mathbf{S}_N = [p_{FOM}(\mathbf{x}, s_1, \mu_1), \dots, p_{FOM}(\mathbf{x}, s_{N_s}, \mu_{N_\mu})], \quad (32)$$

where N_s is the number of complex frequencies. After solving (12), the snapshot matrix can be written as

$$\mathbf{S}_N = \begin{bmatrix} \mathbf{S}_N^\sigma \\ \mathbf{S}_N^\gamma \end{bmatrix} \in \mathbb{R}^{2N \times N_s}, \quad (33)$$

Note that the basis functions are orthogonal and can be generated by the singular value decomposition (SVD) of the snapshot matrix

$$\mathbf{S}_N = \mathbf{U}\mathbf{\Sigma}\mathbf{V}^T. \quad (34)$$

Thus, $\mathbf{\Phi} = [U_1, \dots, U_{N_{rb}}] \in \mathbb{C}^{2N \times N_{rb}}$, where U_i corresponds to the i th singular vector. The singular values in $\mathbf{\Sigma}$, provides information about the reduction of the problem, defined as

$$E/E_0 = \frac{\delta_i}{\sum_{i=1}^N \delta_i}, \quad (35)$$

where $\mathbf{\Sigma} = \text{diag}(\delta_i)$, $i = 1, \dots, N_s$. In practice the number of basis functions N_{rb} can be chosen by a prescribed tolerance ϵ_{POD}

$$I(N_{rb}) = \frac{\sum_{i=1}^{N_{rb}} \delta_i^2}{\sum_{i=1}^N \delta_i^2} \geq 1 - \hat{\epsilon}_{POD}. \quad (36)$$

To preserve the structure of the high-fidelity matrix \mathbf{K} , a symplectic decomposition (PSD) with a symplectic Galerkin projection is used. Specifically, the *cotangent-lift* method introduced in [61], is applied. It ensures a symplectic matrix in block-diagonal form. Thus, the snapshot matrix (33) is now considered in an extended form

$$\mathbf{S}_{Ncl} = [\mathbf{S}_N^\sigma, \mathbf{S}_N^\gamma] \in \mathbb{R}^{N \times 2N_s}, \quad (37)$$

which can be decomposed in the same way as before by using an SVD to recover the corresponding POD basis, defined as $\mathbf{\Phi} = [U_1, \dots, U_{N_{rb}}] \in \mathbb{C}^{N \times N_{rb}}$. Then,

the symplectic basis is constructed as

$$\mathbf{\Phi}_{cl} = \begin{bmatrix} \mathbf{\Phi} & \mathbf{0} \\ \mathbf{0} & \mathbf{\Phi} \end{bmatrix}, \quad (38)$$

where $\mathbf{\Phi}_{cl} \in \mathbb{C}^{2N \times 2N_{rb}}$. As the ROM is built with a Galerkin projection, the solution can be represented as an expansion of POD basis functions that embed the spatial dynamics and the coordinate system in the Laplace domain.

The matrix expression for the real and imaginary parts of (31) is

$$\begin{bmatrix} p_{ROM}^\sigma \\ p_{ROM}^\gamma \end{bmatrix} = \begin{bmatrix} \mathbf{\Phi} a^\sigma \\ \mathbf{\Phi} a^\gamma \end{bmatrix}. \quad (39)$$

Inserting (39) into (10), the problem is similar to (12) but now consists of solving

$$\mathbf{K}_{rb} \begin{bmatrix} a^\sigma \\ a^\gamma \end{bmatrix} = \mathbf{q}_{rb}, \quad (40)$$

where a^σ and a^γ are the real and imaginary part of the solution and q_{rb} is the reduced right hand side function. Moreover $\mathbf{K}_{rb} = \mathbf{\Phi}_{cl}^T \mathbf{K} \mathbf{\Phi}_{cl}$, where

$$\mathbf{K}_{rb} = \begin{bmatrix} \mathbf{\Phi} & \mathbf{0} \\ \mathbf{0} & \mathbf{\Phi} \end{bmatrix}^T \begin{bmatrix} \mathbf{K}^\sigma & -\mathbf{K}^\gamma \\ \mathbf{K}^\gamma & \mathbf{K}^\sigma \end{bmatrix} \begin{bmatrix} \mathbf{\Phi} & \mathbf{0} \\ \mathbf{0} & \mathbf{\Phi} \end{bmatrix}, \quad (41)$$

$$\mathbf{q}_{rb} = \mathbf{\Phi}_{cl}^T \begin{bmatrix} Q^\sigma \\ Q^\gamma \end{bmatrix}. \quad (42)$$

The operator can be written as

$$\mathbf{K}_{rb} = \begin{bmatrix} \mathbf{\Phi} \mathbf{K}^\sigma \mathbf{\Phi}^T & -\mathbf{\Phi}^T \mathbf{K}^\gamma \mathbf{\Phi} \\ \mathbf{\Phi} \mathbf{K}^\gamma \mathbf{\Phi}^T & \mathbf{\Phi}^T \mathbf{K}^\sigma \mathbf{\Phi} \end{bmatrix} = \begin{bmatrix} \mathbf{K}_\Phi^\sigma & -\mathbf{K}_\Phi^\gamma \\ \mathbf{K}_\Phi^\gamma & \mathbf{K}_\Phi^\sigma \end{bmatrix}, \quad (43)$$

where

$$\mathbf{K}_\Phi^\sigma = (\sigma^2 - \gamma^2) \mathcal{M}_\Phi + c^2 \mathcal{S}_\Phi + \sigma \mathcal{B}_\Phi^\sigma, \quad (44a)$$

$$\mathcal{M}_\Phi = \mathbf{\Phi}^T \mathcal{M} \mathbf{\Phi}, \quad (44b)$$

$$\mathbf{K}_\Phi^\gamma = 2\sigma\gamma \mathcal{M}_\Phi + \gamma \mathcal{B}_\Phi^\gamma, \quad (44c)$$

$$\mathcal{S}_\Phi = \mathbf{\Phi}^T \mathcal{S} \mathbf{\Phi}, \quad (44d)$$

$$\mathcal{B}_\Phi^\sigma = \mathbf{\Phi}^T \mathcal{B}^\sigma \mathbf{\Phi}, \quad (44e)$$

$$\mathcal{B}_\Phi^\gamma = \mathbf{\Phi}^T \mathcal{B}^\gamma \mathbf{\Phi}. \quad (44f)$$

For the case where the system is excited with an initial condition the expression becomes

$$\mathbf{q}_{rb} = \begin{bmatrix} \Phi & 0 \\ 0 & \Phi \end{bmatrix}^T \begin{bmatrix} Q^\sigma \\ Q^\gamma \end{bmatrix} = \begin{bmatrix} Q_\Phi^\sigma \\ Q_\Phi^\gamma \end{bmatrix}, \quad (45)$$

where

$$Q_\Phi^\sigma = \sigma \hat{p}_0 \mathcal{M}_{\Phi q}, \quad Q_\Phi^\gamma = \gamma \hat{p}_0 \mathcal{M}_{\Phi q}, \quad (46a)$$

$$\mathcal{M}_{\Phi q} = \Phi^T \mathcal{M}. \quad (46b)$$

130 The solution $[p_{rb}^\sigma, p_{rb}^\gamma]^T$ is finally transformed to the time-domain by applying Weeks method.

For frequency-independent boundary conditions, the parameter μ corresponds to the surface impedance Z_s . It is sampled to generate the snapshots
 135 for every complex frequency so that $\mathbf{S}_N \in \mathbb{R}^{N \times h2N_s}$, where h is the number of sampled impedance values.

The frequency-dependent boundary conditions are treated in a similar way. First, the real and imaginary parts of the pressure are computed from (13).
 140 These values are used in (17), to compute the real and imaginary components of the normal velocity at the boundary. Making use of (22), the admittance at the boundaries is computed. Finally, (40) is solved.

To compare the performance of the ROM against the FOM, the speedup is introduced

$$speedup = \frac{CPU_{FOM}}{CPU_{ROM}}, \quad (47)$$

where CPU_{FOM} is the time needed to solve the FOM for a single parameter
 145 value and CPU_{ROM} the time needed to solve the ROM a single parameter value with the selected number of basis N_{rb} . Note that the speedup measures only the online stage.

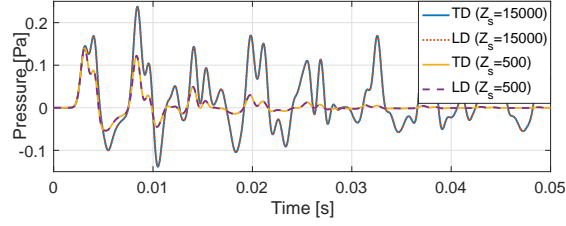
3. Numerical results

We now examine numerical test cases to offer insights into the different
 150 properties of the FOM and ROM.

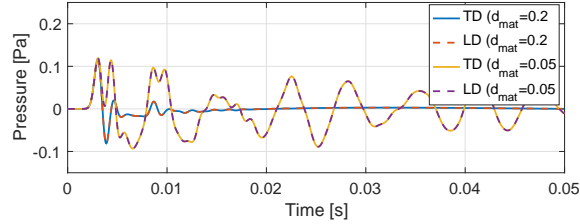
3.1. Full Order Model verification

The Laplace domain SEM for room acoustics is verified via comparisons
 with a time domain SEM solver [6]. First, a 2D domain (2 m \times 2 m) with
 frequency-independent boundary conditions is considered. The number of ele-
 155 ments per Cartesian direction is set to $N_e = 20$ and a basis order of $P = 4$ is
 used ($N = 6561$). The spatial resolution in this case corresponds to roughly 13
 points per wavelength (*PPW*) at 1 kHz. The model is excited with a Gaus-
 sian pulse as initial condition (4) with $\sigma_g = 0.2$ at $(s_x, s_y) = (1, 1)$ m. First,
 the model is tested with frequency-independent boundaries with two surface
 160 impedances of $Z_s = [500 \quad 15000]$ $\text{kgs}^{-1}\text{m}^{-2}$, which correspond to the normal
 incidence absorption coefficient value $\alpha_{norm} = [0.99 \quad 0.10]$. The time step was
 selected following the global Courant-Friedrichs-Lewy (CFL) condition for the
 time-domain solver defined as [6]. The parameters for the Weeks time recon-
 struction when using $N_s = 3000$ are $\sigma = 10$ and $b = 1000$. Figure 1a shows the
 165 impulse responses at $(r_x, r_y) = (0.2, 0.2)$ showing good agreement between the
 two solvers. For the particular case of $Z_s = 15000 \text{ kgs}^{-1}\text{m}^{-2}$, the error at the
 receiver point at $t = 0.1$ s is $\epsilon = |p_{\text{Time}} - p_{\text{Laplace}}| = 8 \times 10^{-5}$ Pa.

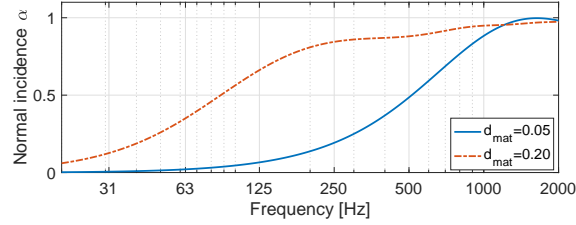
Secondly, frequency-dependent boundaries are considered for the same do-
 main, source and receiver positions and simulation parameters, except that
 170 $N_e = 15$ ($N = 3721$). The boundary is modelled as a porous material mounted
 on a rigid backing. The flow resistivity of the material is $\sigma_{mat} = 10000 \text{ Nsm}^{-4}$
 and the thickness as $d_{mat} = [0.05 \quad 0.2]$ m. The surface impedance are esti-
 mated using Miki's model [54] in conjunction with a transfer matrix method
 [55]. The corresponding absorption coefficient (6) is presented in Figure 1c.
 175 Figure 1b confirms a good match between the two solvers. For the particular
 case of $d_{mat} = 0.05$ m, the error was calculated at the receiver point and $t = 0.05$
 s, as $\epsilon = |p_{\text{Time}} - p_{\text{Laplace}}| = 3 \times 10^{-5}$ Pa.



(a) Frequency-independent boundaries.



(b) Frequency-dependent boundaries.



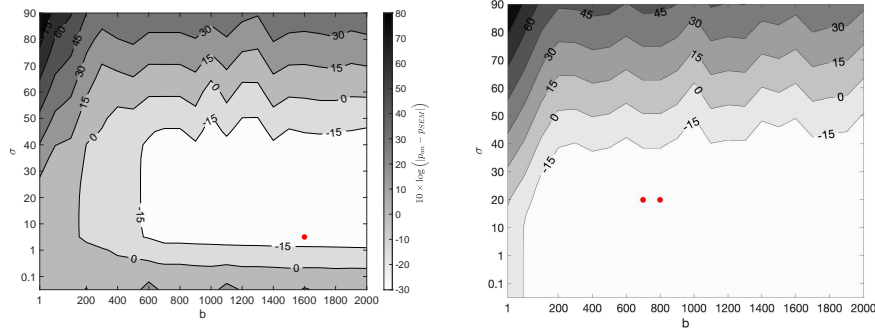
(c) Absorption coefficient for different material thickness d_{mat} (in meters)

Figure 1: FOM impulse response simulations for different parameter values and absorption coefficients. The source location is $(s_x, s_y) = (1, 1)$ m and the receiver location is $(r_x, r_y) = (0.2, 0.2)$ m. Simulations were carried out with $P = 4$, $\Delta t = 5.9 \times 10^{-6}$ s, $N_e = 15$ and $N_e = 20$, $N_s = 3000$ and $(\sigma, b) = (10, 1000)$.

3.1.1. Influence of the Weeks parameters

The free parameters of the Weeks method (σ, b) are identified using (29).
 180 The error is estimated using $N_s = 7000$ and 11 equally spaced points for $\sigma \in [0.1, 2000]$ and 11 equally spaced points for $b \in [0.1, 90]$ for rigid boundary conditions and frequency-independent boundaries with $Z_s = 2000 \text{ kgs}^{-1}\text{m}^{-2}$. Figure 2 shows the results and the pair of parameter values that provide the lowest error are marked with a red dot. Contour lines present the error in
 185 dB given by $10 \log_{10}(|p_{Time} - p_{Laplace}|)$. The parameters can be selected for

those values that lie inside the region where the error is the minimal. For the rigid boundary case this region is smaller, whereas it is found to be larger once some absorption is added at the boundary. As Z_s decreases, i.e., increasing the absorption at the boundaries, the region becomes larger. This finding is good news from an acoustical point of view, as in most cases some absorption is present at the boundary, making the choice of the two free parameters less crucial.



(a) Rigid boundaries with $N_s = 7000$.

(b) $Z_s = 2000 \text{ kgs}^{-1} \text{m}^{-2}$ with $N_s = 7000$.

Figure 2: Contour plot of the error obtained using 11 equally spaced points for $\sigma \in [0.1, 2000]$ and 11 equally spaced points for $b \in [0.1, 90]$ for three different boundary conditions to obtain (29).

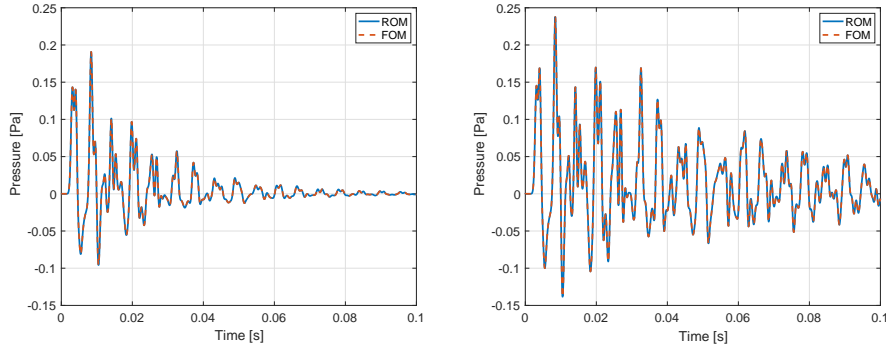
3.2. Reduced Order Model

In this section, the reduced basis method is applied to different test cases to illustrate the potential of the method. The varying parameter of the system is the absorption properties of the boundaries.

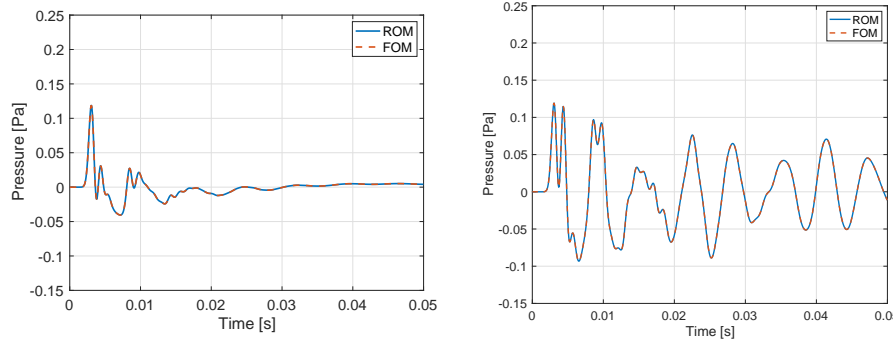
3.2.1. 2D ROM with frequency-independent boundaries

The frequency-independent test case as before is now considered with $N = 6561$, which for a six-elements per wavelength thumb rule [62] the upper frequency is 2 kHz. The ROM is constructed by generating snapshots when sampling the surface impedance values uniformly $Z_s = [500, 1500, 2500, \dots, 15500] \text{ kgs}^{-1} \text{m}^{-2}$.

Figure 3a and Figure 3b show the simulation results with surface impedances of $5000 \text{ kgs}^{-1}\text{m}^{-2}$ and $15000 \text{ kgs}^{-1}\text{m}^{-2}$, that were not included in the snapshot matrix. The corresponding FOM simulations are used for verification. The number of basis functions ($N_{rb} = 300$) were selected using (36) for $\hat{\epsilon}_{POD} = 10^{-6}$. Results show a good match between the ROM and FOM with an absolute error, calculated at the receiver point at $t = 0.1 \text{ s}$ and for $Z_s = 15000 \text{ kgs}^{-1}\text{m}^{-2}$, of $\epsilon = |p_{\text{FOM}} - p_{\text{ROM}}| = 4.3 \times 10^{-9} \text{ Pa}$. The relative error for this particular case is given by $\epsilon_{rel} = \left| \frac{p_{\text{FOM}} - p_{\text{ROM}}}{p_{\text{FOM}}} \right| = 6.5 \times 10^{-7}$.



(a) Frequency-independent boundaries with $Z_s = 5000 \text{ kgs}^{-1}\text{m}^{-2}$ and $N_{rb} = 300$. (b) Frequency-independent boundaries with $Z_s = 15000 \text{ kgs}^{-1}\text{m}^{-2}$ and $N_{rb} = 300$.



(c) Frequency-dependent boundaries with $d = 0.15 \text{ m}$ and $N_{rb} = 150$. (d) Frequency-dependent boundaries with $d = 0.05 \text{ m}$ and $N_{rb} = 150$.

Figure 3: Simulated pressure using the 2D FOM and ROM for different parameter values Z_s and d_{mat} .

The speedup and accuracy of the ROM are investigated by running simu-

lations for different $N_{rb} = [7, 18, 30, 44, 82, 303, 585, 842]$. The singular energy distribution, error, and computational cost are presented as a function of the number of basis functions in Figure 4. The speedup for different number of basis and error values is shown in Figure 5. The convergence for the ROM Laplace solver is demonstrated by looking at the errors as a function of N_{rb} . As expected, including more basis functions to the ROM improves the accuracy but reduces the speedup. The speedup is about 400 when the error is 2×10^{-3} Pa, and 200 for an error of 3×10^{-5} Pa.

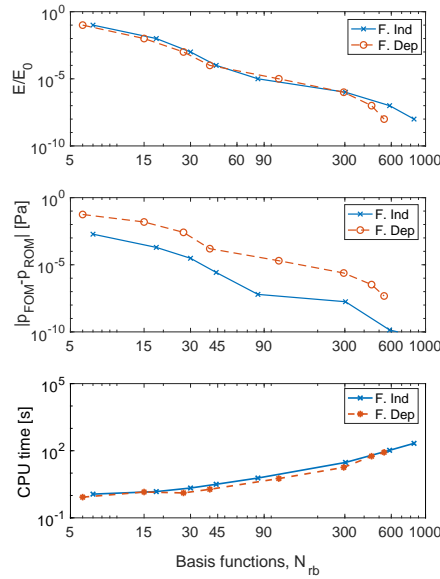


Figure 4: Error and cpu time of the 2D ROM for different basis functions. Simulations were carried out with a fixed $PPW = 13$ for frequency-independent boundaries and $PPW = 10$ for frequency-independent at 1000 Hz, $P = 4$, $Z_s = 5000 \text{ kgs}^{-1} \text{m}^{-2}$ and $d_{mat} = 0.15 \text{ m}$.

220 3.2.2. 2D ROM with frequency-dependent boundaries

The frequency-dependent test case is considered again. The thickness of the modeled material is uniformly sampled to generate the snapshots as $d_{mat} = [0.02, 0.12, 0.22] \text{ m}$.

The results are presented in Figure 3c and Figure 3d for values that were

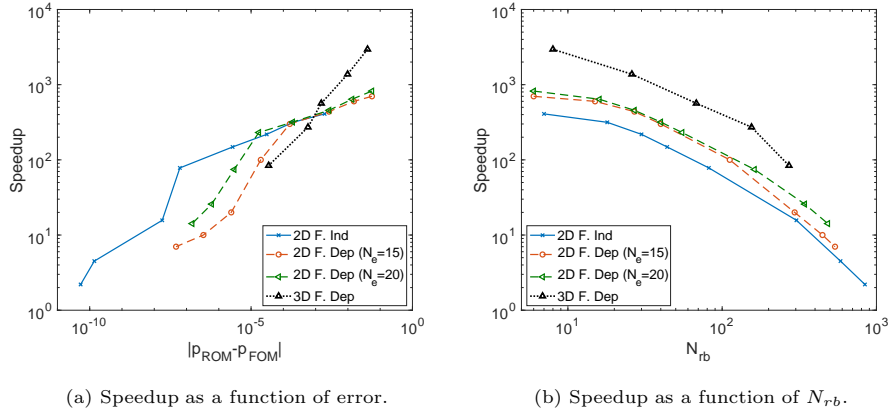


Figure 5: Speedup for 2D and 3D. (a) Speedup as function of error, (b) Speedup as function of N_{rb} .

not sampled to construct the ROM and compared with the corresponding FOM
 high-fidelity solution for verification purposes. The number of basis functions
 ($N_{rb} = 150$) were selected for $\hat{\epsilon}_{POD} = 10^{-6}$. A good match between the ROM
 and FOM shown in Figure 3c and Figure 3d. The absolute error, calculated
 at the receiver point at $t = 0.05$ s and for $d_{mat} = 0.05$ m, is $\epsilon = |p_{FOM} -$
 $p_{ROM}| = 2 \times 10^{-9}$ Pa. Moreover, the relative error for this particular case is
 $\epsilon_{rel} = \frac{|p_{FOM} - p_{ROM}|}{p_{FOM}} = 3.6 \times 10^{-7}$.

The computational cost and speedup for different number of basis and error
 values are presented in Figure 4 and Figure 5, and are similar to the frequency-
 independent case. When $N_e = 15$ ($N = 3725$), the speedup is about 700
 when the error is 5.5×10^{-2} Pa, and reduces to 100 for an error of 2×10^{-5}
 Pa. A second ROM with $N_e = 20$ ($N = 6561$) is constructed to compare
 the effect of increasing the DOF. Figure 5 shows that the ROM constructed
 with $N_e = 20$ results in to higher speedups than the ROM with $N_e = 15$.
 Note that Figure 5 shows different speedup values for the frequency-independent
 and frequency-dependent cases. The reason is that the computational time of
 the FOM is higher for the frequency-dependent case, which leads into different
 speedup values.

3.2.3. 3D cube ROM with frequency-dependent boundaries

This section considers a 3D 1 m \times 1 m \times 1 m cube shaped room. A ROM with
245 frequency-dependent boundaries is constructed. The boundaries are modeled
using Miki's model [54], with a flow resistivity of $\sigma_{mat} = 10000 \text{ Nsm}^{-4}$, where
the material thickness $d_{mat} = [0.02, 0.12, 0.22] \text{ m}$ is parametrized to create
the ROM. The simulations are carried out using a number of elements per
direction of $N_e = 8$ and $P = 4$ ($N = 35937$). Assuming a fixed number
250 of points per wavelength of $PPW = 10$, the upper frequency limit is 1 kHz.
The initial condition is a Gaussian pulse with $\sigma_g = 0.2 \text{ m}^2$. The source is
placed at $(s_x, s_y, s_z) = (0.5, 0.5, 0.5) \text{ m}$ and the receiver is placed at $(r_x, r_y, r_z) =$
 $(0.25, 0.1, 0.8) \text{ m}$. For this case, the number of frequencies is chosen to be $N_s =$
1800 and the Week parameters are $\sigma = 20$ and $b = 800$. Figure 6 shows the
255 verification of the 3D solver against a time domain solver [6] and the resulted
ROM for $d_{mat} = 0.05 \text{ m}$ and $N_{rb} = 155$. For this particular case, the error
between the FOM and the ROM is $5.8 \times 10^{-4} \text{ Pa}$.

During the online phase of the RBM, different ROMs are built to compare the
error and the speedup against the FOM. Figure 5 shows the speedup of the
260 ROM for different error values compared with the 2D cases. Results show a
speedup between two and three orders of magnitude depending on the error
tolerance chosen. The speedup is more than 1000 when the error tolerance is
almost 10^{-2} , and reduces to 100 for an error tolerance of 10^{-5} . Note that the
error for the 3D case in Figure 5a is larger compared to the 2D cases due to
265 a lower number of elements per direction N_e and thus, a lower resolution. A
better comparison is shown in Figure 5b where the speedup is higher for the 3D
case for the same number of basis.

The ROM constructed with three FOM simulations for different values of
 d_{mat} , requires 8GB of storage. The performance of the ROM including the
270 offline stage cost is analyzed. The ROM is constructed with three FOM simu-
lations for different values of d_{mat} . Thus, the computational time of the ROM
begin after the time taken by the three FOM simulations. Figure 7 shows the

computational cost of the FOM and ROM with different N_{rb} . As an example, four different parameter values, d_{mat} , per surface need to be simulated, which leads to a total number of 4096 simulations to explore all the possibilities. For the case where $N_{rb} = 40$, the ROM is three orders of magnitude faster than the FOM with an error equal to 2.9×10^{-3} Pa. A singular energy decay analysis revealed that most energy is concentrated within the first 1185 basis function, so the reduced model with $N_{rb} > 1185$ does not significantly improve the error as shown in Figure 7). Thus, in this case, the interest is to construct a ROM with $N_{rb} < 1185$ and probably much smaller. Note that the offline stage consist of FOM simulations that are independent to each other. Thus, the computational time of this stage can be reduced, e.g., computing the FOM for different parameter values in parallel.

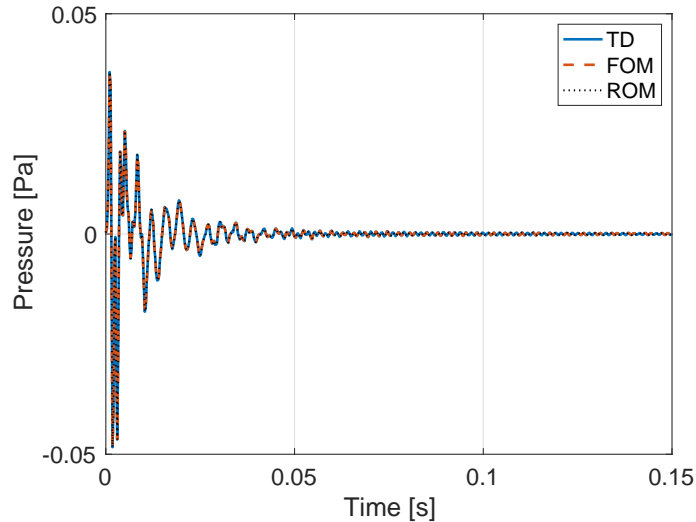


Figure 6: 3D TD, LD FOM and ROM impulse response simulations. The source location is $(s_x, s_y, s_z) = (0.5, 0.5, 0.5)$ m and the receiver location is $(r_x, r_y, r_z) = (0.25, 0.1, 0.8)$ m. Simulations were carried out with $P = 4$, $N_e = 8$, $N_s = 1800$, $(\sigma, b) = (20, 800)$ and $N_{rb} = 155$.

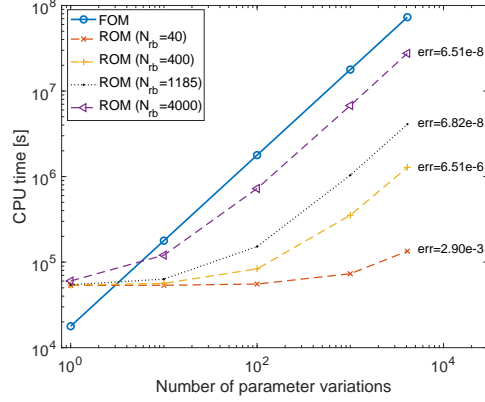


Figure 7: Computational cost of ROM including offline stage.

285 *3.2.4. Effects on the singular values decay and number of sampled parameters*

To understand the RBM behavior in more details, we test additional conditions 1) different domain size in 2D, 2) number of complex frequencies in 2D, 3) number of sampled parameters. The effects of these changes on the singular value energy decay are studied in Figure 8. Figure 8a shows the results when
 290 fixing the $PPW = 10$ at 1000 kHz. The number of basis functions needed to include a certain energy value decreases with increasing dimensions of the domain. In other words, the size of the ROM becomes smaller compared to the FOM when increasing the domain. Table 1 shows an example of the reduction in DOF_{ROM} compared to DOF_{FOM} for $\hat{\epsilon}_{POD} = 10^{-6}$, which varies from from
 295 45.2% to 8.2% when the edge length increases from 1 m to 4 m. The basis functions needed to capture the correct acoustics when making the domain larger do not increase as rapidly as the increase of the DOFs.

In Figure 8b, the number of elements per direction is fixed to $N_e = 20$. When increasing the size of the domain, the number of basis functions needed
 300 increases due to the low resolution. Note that in such cases, the number of PPW decreases when increasing the size of the domain. Figure 8c shows that the basis functions needed to include certain energy value increases when increasing N_s . The longer the simulation time is, the more complex frequencies are needed.

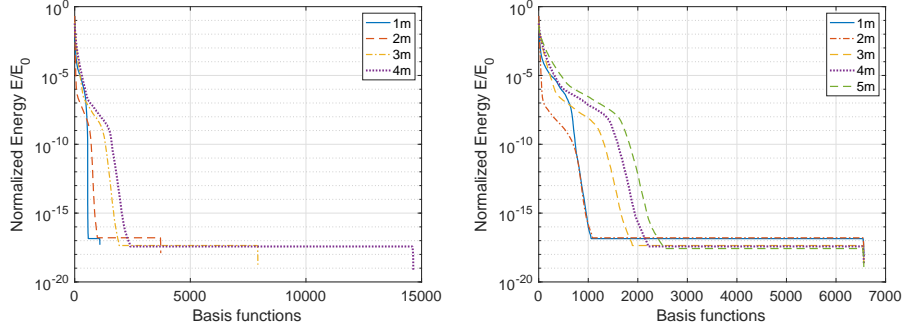
Thus, more basis functions are needed to capture the wave propagation over
 305 longer time.

We investigated the effects of the number of offline calculations for the FOM
 parameter sampling, N_{snap} , on the energy decay in Figure 8d. A slower energy
 decay is observed when N_{snap} is increased, meaning the the size of ROM gets
 larger. Because the upfront offline cost is expensive as $\mathcal{O}(N_{snap})$, we additionally
 310 investigated how the error of the ROM using the corresponding N_{snap} varies as
 a function of Z_s values in Figure 9 defined as $\epsilon = |p_{FOM} - p_{ROM}|$ computed at
 $t = 0.1$ s in the receiver point $(r_x, r_y) = (0.2, 0.2)$ m. For most Z_s values, the ROM
 with more number of N_{snap} are more accurate, but with a reasonable accuracy
 tolerance of 10^{-4} , N_{snap} of 3 is acceptable. For this particular case, increasing
 315 N_{snap} decreases the error for most Z_s values. However, it depends on the error
 tolerance. Moreover, the computational time of the offline stage increases with
 $\mathcal{O}(N_{snap})$. The results show that for a uniform sampling strategy, increasing
 N_{snap} produces a slower energy decay of the singular values (Figure 8d), an
 increased accuracy (Figure 9) and an increase of the offline computational time.
 320 It can be seen that with $N_{snap} = 3$ the acoustics of the system can be captured
 accurately to cover the whole practical range of interest of the parametrized
 surface impedance. This suggests that the RBM approach is more beneficial
 when solving large scale problems, which is the case in room acoustics.

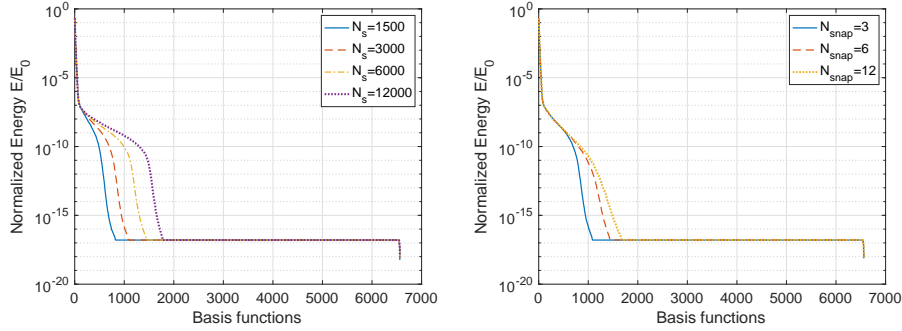
Table 1: DOF_{ROM}/DOF_{FOM} in percentage for $\hat{\epsilon}_{POD} = 1 \times 10^{-6}$.

Domain side length	1 m	2 m	3 m	4 m
DOF_{ROM}/DOF_{FOM}	45.2%	12.3%	11.9%	8.2%

The same analysis has been done for frequency-dependent boundaries. Re-
 325 sults are similar to those as described for the frequency-independent case.



(a) Energy decay for different domain side lengths with a fixed $PPW = 10$ at 1000 Hz. (b) Energy decay for different domain lengths with a fixed number of elements $N_e = 20$.



(c) Energy decay for different number of complex frequencies N_s . (d) Energy decay for different number of sampled parameters.

Figure 8: Illustration of computed singular value decay as a measure of the Kolmogorov n -width for different scenarios based on a square domain of size $2\text{ m} \times 2\text{ m}$ with frequency-independent BC. $N_e = 20$, $t = 0.1\text{ s}$, $N_s = 3000$ and $N_{snap} = 3$.

3.2.5. Computational cost and storage

An analysis of the computational and storage cost of the previously presented 2D ROM with frequency-dependent boundary conditions is performed. Figure 10a presents the computational time of the FOM for different DOF where it can be seen that the CPU time increases when increasing N as $\mathcal{O}(N)$. Moreover, Figure 10b shows the computational cost in seconds for each FOM sampled parameter as a function of the upper limit frequency given by the element size. For this analysis, a polynomial order of $P = 4$ and a six-elements per wavelength thumb rule is considered [62]. Note that in order to know the total cost of all the

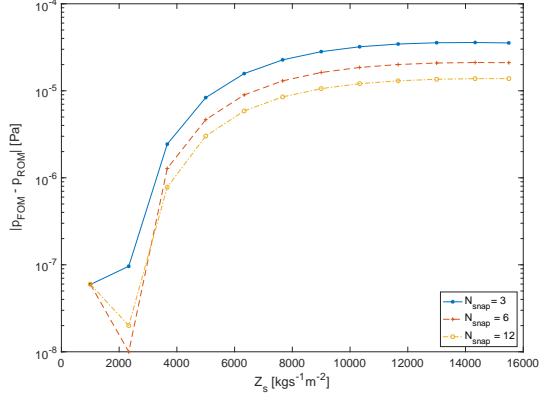
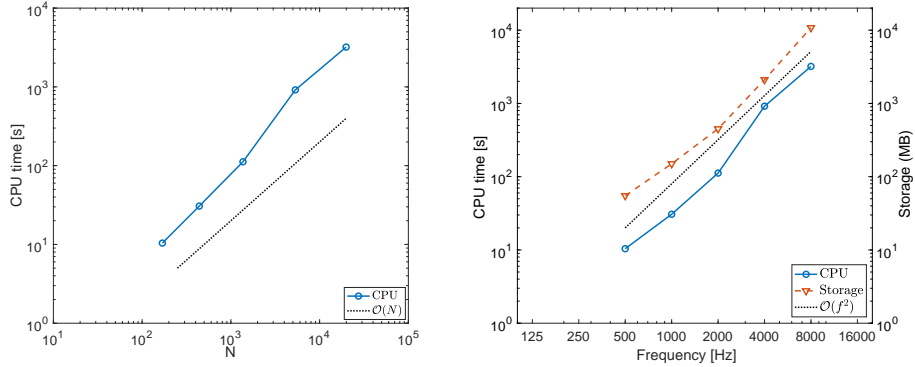


Figure 9: Error between ROM and FOM for different parameter values and N_{snap} using $N_{rb} = 44$ and $\hat{\epsilon}_{POD} = 10^{-4}$.

335 snapshots, the values need to be multiplied by the number of snapshots. The results show that the CPU time is increasing as $\mathcal{O}(f^2)$. Moreover, the storage of ROM including all the snapshots is also plotted, which increases as a quadratic function of f . The dependency with the number of complex frequencies N_s is straightforward. Changing N_s by a factor x will scale results in Figure 10 x
340 times.

4. Analysis and discussion

The ROM developed for room acoustic simulations concurs with previous work from other disciplines, e.g., [63–65], in terms of speedup factors with respect to the error. A speedup of 100 is found with an error level of 6×10^{-8}
345 Pa and 2×10^{-5} Pa for 2D frequency-independent and frequency-dependent, respectively. For the 3D frequency-dependent case, a speedup of 300 is found when the error is 6×10^{-4} Pa and 1300 for an error value equal to 9.8×10^{-3} Pa. It is clear that a compromise between the desired error and the speedup occurs. In room acoustics, the impulse response is used to characterize a room
350 for a given source and receiver position. One of the more important acoustic parameters is the reverberation time, T_{30} or T_{20} , defined in ISO 3382-1 [66],



(a) CPU time of the FOM for different degree of freedom. (b) CPU and storage of the ROM for different frequency limits.

Figure 10: Computational and storage cost for frequency-dependent 2D case. Simulations were carried out with a fixed $PPW = 6$ and $P = 4$.

which can be obtained from the impulse response and is commonly used for evaluating the acoustic conditions of an enclosure. The precision needed to calculate reverberation times is related to the dynamic range of the signal given by the background noise. For T_{30} and T_{20} , a background noise level of -45 dB and -35 dB respectively is needed [66], which correspond to errors of 5.6×10^{-3} and 1.77×10^{-2} . For sound pressure level (SPL) prediction, the just noticeable difference for a broadband noise is 1 dB, which amount to about 11% error.

Results show a potential speedup when increasing the size of the problem or N as shown in Figure 5, so mostly beneficial for large 3D domains. Figure 10a shows how the computational time of the 2D FOM increases when N grows. On the other hand, increasing N could be a problem in terms of memory storage. However, Figure 10b shows affordable storage values for the presented cases. It is found that for the analyzed 2D case, 2GB of storage is needed for an upper frequency of 4 kHz and 10.8GB for 8 kHz. Moreover, the singular value decay analysis shows a potential benefit for large rooms Figure 8. In the analogous 3D case, 8GB of storage is needed for an upper frequency of 1kHz. All these results show favorable conditions for room acoustics with reasonable domain sizes.

The main drawback of the current work is that constructing the impulse
370 response is time-consuming due to the parameter search for the Weeks method.
The optimal choice of the Weeks parameter also depends on N_s , and it is case
dependent. It is relieving that larger optimal parameter ranges exist for non-
rigid boundary condition, as many practical building materials are acoustically
non-rigid.

375 A future work is to investigate this further and develop a more efficient
method to estimate the parameters. Moreover, the framework will be extended
in future work by focusing on larger domains for realistic 3D cases. Parallel
and high-performance computing techniques are also candidates to overcome
the extra computational cost for those complex and larger scenarios.

380 5. Conclusion

This study evaluates the potential of using RBM techniques for parametrized
boundaries in room acoustic simulations. The proposed framework reduces the
problem to a low dimensional subspace aiming a computational reduction using
a Laplace domain ROM on a high fidelity SEM solver, including complex bound-
385 ary conditions. The solution is finally transformed back to the time-domain to
reconstruct the impulse responses. The test cases presented in this paper show
the potential of this framework for room acoustics simulations. A typical sce-
nario is to simulate iteratively a room for different absorption properties of the
boundaries to find the optimal values that fulfil a pre-defined acoustic require-
390 ment. It is shown that the ROM enables simulating different parameter values
of the boundaries at a significantly lower cost compared to the FOM. Results
confirm that the use of RBM decreases the simulation time by at least two or-
der of magnitude for the 2D cases presented here and three order of magnitude
for the 3D cases, including the frequency-independent and dependent boundary
395 conditions. The speedup including the offline stage, where the ROM is con-
structed by sampling the parameter variations on the FOM, is three orders of
magnitude faster than the FOM when four different boundary conditions are

simulated per room surface in a 3D case with frequency-dependent boundaries.

Results show favourable behaviour in terms of speedup when increasing the
400 size of the domain, indicating a potential further accelerations for larger do-
mains. Moreover, a memory storage is manageable for the tested cases, albeit
small, for a unit cube. This suggests that the presented framework is expected
to be most useful for larger scale engineering problems, such as building design
and renovation.

405 A challenge is on the choice of the number of complex frequencies and the
free parameters to construct the impulse response by means of Weeks method.
However, results show that for a room with damped boundaries, broader ranges
of the Weeks parameters ensure good accuracy, which is relevant for room acous-
tics as absorption at the boundaries is always included.

410 **Acknowledgments**

This work is partly supported by Innovationsfonden, Denmark (Grant ID
9065-00115B), Rambøll Danmark A/S and Saint-Gobain Ecophon A/S, Sweden.

References

- [1] L. Savioja, U. P. Svensson, Overview of geometrical room acoustic modeling
415 techniques, *J. Acoust. Soc Am.* 138 (2) (2015) 708–730.
- [2] M. Vorlaender, *Fundamentals of Acoustics, Modelling, Simulation, Algo-
rithms and Acoustic*, Springer International Publishing, 2020.
- [3] F. Brinkmann, L. Aspöck, D. Ackermann, S. Lepa, M. Vorländer,
S. Weinzierl, A round robin on room acoustical simulation and auralization,
420 *J. Acoust. Soc. Am.* 145 (4) (2019) 2746–2760.
- [4] A. Craggs, A finite element method for free vibration of air in ducts and
rooms with absorbing walls, *J. Sound Vib* 73 (4) (1994) 568–576.

- [5] T. Okuzono, K. Sakagami, A frequency domain finite element solver for acoustic simulations of 3D rooms with microperforated panel absorbers, *Applied Acoustics* 129 (2018) 1–12.
- [6] F. Pind, A. P. Engsig-Karup, C. H. Jeong, J. S. Hesthaven, M. S. Mejlum, J. S. Andersen, Time domain room acoustic simulations using the spectral element method, *J. Acoust. Soc. Am* 145 (6) (2019) 3299–3310.
- [7] D. Botteldooren, Finite-difference time-domain simulation of low-frequency room acoustic problems, *J. Acoust. Soc. Am* 98 (6) (1995) 3302–3308.
- [8] J. A. Hargreaves, L. R. Rendell, Y. W. Lam, A framework for auralization of boundary element method simulations including source and receiver directivity, *J. Acoust. Soc. Am* 145 (4) (2019) 2625–2637.
- [9] H. Wang, I. Sihar, R. P. Munoz, M. Hornikx, Room acoustics modelling in the time-domain with the nodal discontinuous Galerkin method, *J. Acoust. Soc. Am.* 145 (4) (2019) 2650–2663.
- [10] H.-O. Kreiss, J. Olinger, Comparison of accurate methods for the integration of hyperbolic equations, *Tellus* 24 (3) (1972) 199–215.
- [11] S. Sherwin, Dispersion analysis of the continuous and discontinuous Galerkin formulations, Springer, Berlin, Heidelberg, 2000.
- [12] G. Gassner, D. Kopriva, A comparison of the dispersion and dissipation errors of gauss and gauss-lobatto discontinuous galerkin spectral element methods, *SIAM Sci. Comp.* 33 (5) (2011) 2560–2579.
- [13] M. Ainsworth, H. Wajid, Dispersive and dissipative behavior of the spectral element method, *SIAM J. Numer. Anal.* 47 (5) (2009) 3910–3937.
- [14] A. van de Walle, F. Naets, E. Deckers, W. Desmet, Stability preserving model order reduction for time-domain simulation of vibro-acoustic FE models, *Int. J. Num. Meth. Eng.* 109 (6) (2017) 889–912.

- [15] B. Moore, Principal component analysis in linear systems: Controllability, observability, and model reduction, *IEEE Trans. Automat. Control* 26 (1) (1981) 17–32.
- [16] D. Amsallem, C-Farhat, Stabilization of projection-based reduced-order models, *J. Num. Meth. Eng.* 91 (4) (2012) 358–377.
- [17] I. Kalashnikova, B. van Bloemen Waanders, S. Arunajatesanand, M. Barone., Stabilization of projection-based reduced-order models for linear time-variant systems via optimization-based eigenvalue reassignment, *Comput. Meth. Appl. Mech. Eng.* 272 (1) (2014) 251–270.
- [18] B. Cockburn, C.-W. Shu, The local discontinuous galerkin method for time-dependent convection diffusion system, *SIAM J.* 35 (0) (1998) 2440–2463.
- [19] B. Cockburn, C.-W. Shu, Runge-kutta discontinuous galerkin methods for convection-dominated problems, *J. Sci. Comput* 16 (3) (2001) 173–261.
- [20] J. S. Hesthaven, G. Rozza, B. Stamm, *Certified Reduced Basis Methods for Parametrized Partial Differential Equations*, Springer, 2016.
- [21] A. Quarteroni, G. Rozza, A. Manzoni, Certified reduced basis approximation for parametrized partial differential equations and applications, *J. Math Ind* 1 (3) (2011) .
- [22] N. N. Cuong, K. Veroy, A. T. Patera, Certified real-time solution of parametrized partial differential equations, *Handbook of Materials Modeling*, 2005, pp. 1529-1564.
- [23] G. Rozza, D. B. P. Huynh, A. T. Patera, Reduced basis approximation and a posteriori error estimation for affinely parametrized elliptic coercive partial differential equations, *Archives of Computational Methods in Engineering* 15 (3) (2008) 229–275.
- [24] M. Drohmann, K. Carlberg, The ROMES method for statistical modeling of reduced-order-model error, *SIAM/ASA J. on Uncer. Quant.* 3 (1) (2015) 116–145.

- [25] C. Prud'homme, A. Patera, Reduced-basis output bounds for approximately parametrized elliptic coercive partial differential equations, *Computing and Visualization in Science* 6 (2-3) (2004) 147–162.
- 480 [26] A. Quarteroni, A. Manzoni, F. Negri, *Reduced Basis Methods for Partial Differential Equations: An Introduction*, Springer, 2015.
- [27] G. Berkooz, P. Holmes, J. L. Lumleyand, C. W. Rowley, *Turbulence, Coherent Structures, Dynamical Systems and Symmetry*, Cambridge University Press, 1996.
- 485 [28] M. Ohlberger, S. Rave, Reduced basis methods: Success, limitations and future challenges, *Proceedings Of The Conference Algoritmy*, 1-12 (2016).
- [29] D. Amsallem, J. Cortial, C. Farhat, Towards realtime computational-fluid-dynamics-based aeroelastic computations using a database of reduced-order information, *AIAA J.*, 48 (9) (2010) 2029–2037.
- 490 [30] S. Giere, Numerical and analytical aspects of pod-based reduced-order modeling in computational fluid dynamics, PhD thesis, Free University of Berlin, Germany (2016).
- [31] M. Ganesh, J. Hesthaven, B. Stamm, A reduced basis method for electromagnetic scattering by multiple particles in three dimensions, *J. Comput. Physics* 231 (23) (2012) 7756–7779.
- 495 [32] Y. Chen, J. S. Hesthaven, Certified reduced basis methods and output bounds for the harmonic maxwell's equations, *SIAM J. Sci. Comput.*, 32 (2) (2010) 970–996.
- [33] M. A. Grepl, Reduced-basis approximation and a posteriori error estimation for parabolic partial differential equations, PhD thesis, Massachusetts Institute of Technology, United States (2005).
- 500 [34] R. S. Puri, D. Morrey, A. J. Bell, J. F. Durodola, E. B. Rudnyi, J. G. Korvink, Reduced order fully coupled structural– acoustic analysis via implicit moment matching, *Appl. Math. Mod* 33 (11) (2009) 4097–4119.

- 505 [35] U. Hetmaniuk, R. Tezaur, C. Farhat, Review and assessment of interpolatory model order reduction methods for frequency response structural dynamics and acoustics problems, *Int. J. Num. Meth. Eng.* 90 (13) (2012) 1636–1662.
- [36] J. Herrmann, M. Maess, L. Gaul, Substructuring including interface reduction for the efficient vibro-acoustic simulation of fluid-filled piping systems, 510 *Mech. Sys. Sig. Proc* 24 (1) (2010) 153–163.
- [37] M. MillerIII, S. van Ophem, E. Deckers, W. Desmet, Time-domain impedance boundary conditions for acoustic reduced order finite element simulations, *Comp. Meth. Appl. Mech. Eng.* 387 (15) (2021) 114173.
- 515 [38] C. Bigoni, J. S. Hesthaven, Simulation-based anomaly detection and damage localization: an application to structural health monitoring, *Comput. Meth. Appl. Mech. Eng* 63 (2020) 12896.
- [39] B. M. Afkham, J. S. Hesthaven, Structure preserving model reduction of parametric hamiltonian systems, *SIAM J. Sci. Comput.* 339 (6) (2017) 520 A2616–A2644.
- [40] V. Pereyra, B. Kaelin, Fast wave propagation by model order reduction, *Elec. Trans. Num. Anal* 30 (-) (2008) 406–419.
- [41] V. Pereyra, Wave equation simulation in two-dimensions using a compressed modeler, *Am. J. Comp. Math.*, 3 (-) (2013) 231–241.
- 525 [42] V. Pereyra, Model order reduction with oblique projections for large scale wave propagation, *Am. J. Comp. Math.*, 295 (-) (2016) 103–114.
- [43] B. Moore, Principal component analysis in linear systems: Controllability, observability, and model reduction, *IEEE Trans. Automat. Control* 26 (1) (1981) 17–32.
- 530 [44] D. Amsallem, C. Farhat, Stabilization of projection-based reduced-order models., *Int. J. Num. Meth. Eng.* 91 (4) (2012) 358–377.

- [45] I. Kalashnikova, B. B. Waanders, A. S., M. Barone, Stabilization of projection-based reduced order models for linear time-invariant systems via optimization based eigenvalue reassignment, *Comput. Meth. Appl. Mech. Eng* 272 (2014) 251–270.
- [46] ISO, Acoustics-Measurement of room acoustic parameters-Part 1: Performance spaces, Standard, International Organization for Standardization - ISO/TC 43/SC 2 Building acoustics (Jun. 2009).
- [47] M. W. Hess, G. Rozza, A Spectral Element Reduced Basis Method in Parametric CFD, *Numerical Mathematics and Advanced Applications – ENUMATH 2017*, Springer, in press, ArXiv e-print 1712.06432, 2017.
- [48] M. W. Hess, A. Alla, A. Q. G. Rozza, M. Gunzburger, A spectral element reduced basis method for Navier–Stokes equations with geometric variations, *ICOSAHOM Conference Proceeding*. Submitted. ArXiv preprint 1812.11051 (2018).
- [49] H. Kuttruff, *Room Acoustics*, 5th Edition, Taylor & Francis, 2009, ch. 2.
- [50] J. S. Hesthaven, T. Warburton, *Nodal Discontinuous Galerkin Methods—Algorithms*, Springer, New York, 2008.
- [51] H. Xu, C. Cantwell, C. Monteserin, C. Eskilsson, A. P. Engsig-Karup, S. Sherwin, Spectral/hp element methods: Recent developments, applications, and perspectives, *Journal of Hydrodynamics* 30 (1) (2018) 1–22.
- [52] B. Cotté, P. Blanc-Benon, C. Bogey, F. Poisson, Time-domain impedance boundary conditions for simulations of outdoor sound propagation, *AIAA Journal* 47 (2009) 10.
- [53] R. Troian, D. Dragna, C. Bailly, M.-A. Galland, Broadband liner impedance eduction for multimodal acoustic propagation in the presence of a mean flow, *J. Sound Vib.* 392 (2017) 200–216.

- [54] Y. Miki, Acoustical properties of porous materials—modifications of delany-bazley models, *J. Acoust. Soc. Jpn.* 11 (1) (1990) 19.24.
- 560 [55] J. F. Allard, N. Atalla, *Propagation of Sound in Porous Media: Modelling sound absorbing materials*, 3rd Edition, Wiley, West Sussex, 2009.
- [56] B. Gustavsen, A. Semlyen, Rational approximation of frequency domain responses by vector fitting, *IEEE Trans. Power Delivery* 14 (3) (1999) 1052–1061.
- 565 [57] W. T. Weeks, Numerical inversion of laplace transform using Laguerre functions, *J. Assc. Comp. Mach.* 13 (3) (1966) 419–429.
- [58] C. Clenshaw, A note on the summation of chebyshev series, *Math. Comp.* 9 (51) (1955) 118–120.
- [59] R. Piessens, B. Maria, Numerical inversion of the laplace transform using
570 generalised laguerre polynomials, *Proceedings of the Institution of Electrical Engineers*, Vol. 118, IET, pp. 1517-1522 (1971).
- [60] B. Garbow, G. Giunta, J. Lyness, Software for an implementation of Weeks’ method for the inverse laplace transform, *ACM Trans. Math. Softw. (TOMS)* 14 (2) (1988) 163–170.
- 575 [61] L. Peng, K. Mohseni, Symplectic model reduction of hamiltonian systems, *SIAM J. Sci. Comput.* 38 (1) (2016) A1–A27.
- [62] N. Atalla, F. Sgard, *Solving uncoupled structural acoustics and vibration problems using the finite element method*, 1st Edition, *Finite Element and Boundary Methods in Structural Acoustics and Vibration*, CRC Press,
580 Boca Raton, 2015.
- [63] J. Pomplun, F. Schmidt, Accelerated a posteriori error estimation for the reduced basis method with application to 3d electromagnetic scattering problems, *SIAM/ASA J. on Sci. Comp.* 32 (2) (2010) 498–520.

- [64] G. Pitton, G. Rozza, On the application of Reduced Basis Methods to
585 Bifurcation Problems in Incompressible fluid dynamics, *J. of Sci. Comp.* 73
(2017) 157–177.
- [65] D. P. Huynh, D. J.Knezevic, A. T.Patera, A Laplace transform certified
reduced basis method; application to the heat equation and wave equation,
Comptes Rendus Mathematique 349 (7-8) (2011) 401–405.
- 590 [66] EN ISO 3382-1:2009, Measurement of room acoustic parameters, part 1:
Performance spaces., Standard, International Organization for Standard-
ization (Dec. 2009).

Nomenclature

595	(r_x, r_y, r_z)	Receiver position
	(s_x, s_y, s_z)	Source position
	α_{norm}	Normal incidence absorption coefficient
	$\hat{\mathbf{v}}$	Particle velocity in time-domain
	Ψ	Simplectic truncated reduced basis
600	Ψ	Truncated reduced basis
	\mathbf{G}	Matrix operator for accumulators
	\mathbf{K}	Matrix operator
	\mathbf{K}_{rb}	Reduced matrix operator
	\mathbf{n}	Outward pointing normal vector of the boundary
605	\mathbf{p}	Sound pressure vector in Laplace domain
	\mathbf{Q}	Right hand side vector
	\mathbf{q}_{rb}	Reduced right hand side vector
	$\mathbf{S}_{\mathcal{N}}$	Snapshot matrix
	$\mathbf{S}_{\mathcal{N}cl}$	Simplectic snapshot matrix
610	\mathbf{v}	Particle velocity in Laplace domain
	\mathbf{x}	Cartesian coordinates in the domain
	\mathbf{x}_0	Source position for the initial condition
	Δt	Time step

	δ	Singular values
615	Γ	Boundary of the domain Ω
	γ	Imaginary part of the complex frequency
	$\hat{\alpha}_k, \hat{\beta}_k$	Complex poles
	$\hat{\lambda}$	Real poles
	$\hat{\phi}_k, \hat{\psi}_k^{(1)}, \hat{\psi}_k^{(2)}$	Accumulators
620	\hat{a}_k	Coefficients for Weeks method
	\hat{p}	Sound pressure in time-domain
	\hat{p}_i^*	Solution simulated with time-domain solver
	\hat{p}_0	Initial condition in time-domain
	\hat{p}_{t_0}	Sound pressure derivative in $t=0$ s
625	\mathbf{G}	Matrix operator for the accumulators
	\mathcal{B}	Boundary matrix
	\mathcal{B}_Φ	Reduced boundary matrix
	\mathcal{M}	Mass matrix
	\mathcal{M}_Γ	Mass matrix for the boundary
630	\mathcal{M}_Φ	Reduced mass matrix
	\mathcal{S}	Stiffness matrix
	$\mathcal{S}_x, \mathcal{S}_y, \mathcal{S}_z$	Stiffness matrix, where x,y,z denote differentiation
	\mathcal{S}_Φ	Reduced stiffness matrix
	μ	Parameter for RBM
635	Ω	Domain

	ϕ_i	Reduced basis
	ρ	Density of the medium (air)
	σ	Real part of the complex frequency
	σ^{opt}	Optimal value of the free parameter
640	σ_g	Spatial variance of the Gaussian pulse
	σ_{mat}	Flow resistivity of porous material
	M	Solution Manifold
	a_i	Reduced basis solution coefficient
	A_k, B_k, C_k	Coefficients
645	a_Q	Zeros of the rational function
	b	Weak free parameter
	b^{opt}	Optimal value of the free parameter
	b_Q	Poles of the rational function
	c	Speed of the sound
650	d_{mat}	Porous material thickness
	E/E_0	Normalized energy of the singular values
	$I(N_{rb})$	Indicator for determining N_{rb} for a given tolerance $\hat{\epsilon}_{\epsilon}POD$
	L	Number of real poles
	$L_k(\cdot)$	Laguerre polynomials of degree k
655	N	Number of degree of freedom
	N_e	Number of elements per direction
	N_s	Number of complex frequencies

	N_t	Number of time steps
	N_{rb}	Number of reduced basis
660	N_{snap}	Number of sampled parameters
	N_s	Number of complex frequencies s
	P	Polynomial order for SEM
	p	Sound pressure in the Laplace domain
	p_i^*	Solution simulated with Laplace domain solver
665	p_Γ	Sound pressure in the Laplace domain at the boundary
	p_{FOM}	High-fidelity solutions
	p_{ROM}	Reduced basis solution
	Q	Order of the rational function
	S	Number of complex poles
670	s	Complex frequency of the Laplace domain
	s_j	j th complex frequency
	T	Final time
	t	Time
	v_n	Normal velocity at the boundary
675	w	Test function
	Y_s	Surface admittance
	Z_s	Surface impedance

This figure "Param_z2000_grayOK2.jpg" is available in "jpg" format from:

<http://arxiv.org/ps/2103.11730v2>